3D-nanoprinted on-chip antiresonant waveguide with hollow core and microgaps for integrated optofluidic spectroscopy

JISOO KIM,[1,2] JOHANNES BÜRGER,[3] BUMJOON JANG,[1,2] MATTHIAS ZEISBERGER,[1] JULIAN GARGIULO,[3] LEONARDO DE S. MENEZES,[3,4] STEFAN A. MAIER,[3,5,6] AND MARKUS A. SCHMIDT[1,2,7,*]

[1]*Leibniz Institute of Photonic Technology, Albert-Einstein-Str. 9, 07745 Jena, Germany*
[2]*Abbe Center of Photnics and Faculty of Physics, Friedrich-Schiller University Jena, Max-Wien-Platz 1, 07743 Jena, Germany*
[3]*Chair in Hybrid Nanosystems, Nanoinstitute Munich, Ludwig-Maximilians-Universität Munich, Königinstraße 10, 80539 Munich, Germany*
[4]*Departmento de Fisica, Universidade Federal de Pernambuco, 50670-901 Recife- PE, Brazil*
[5]*The Blackett Laboratory, Department of Physics, Imperial College London, London SW7 2AZ, United Kingdom*
[6] *School of Physics and Astronomy, Monash University, Clayton, Victoria 3800, Australia*
[7] *Otto Schott Institute of Materials Research (OSIM), Friedrich-Schiller University Jena, Fraunhoferstr. 6, 07743 Jena, Germany*
[*]markus.schmidt@leibniz-ipht.de

Abstract: Here, we unlock the properties of the recently introduced on-chip hollow-core microgap waveguide in the context of optofluidics which allows for intense light-water interaction over long lengths with fast response times. The nanoprinted waveguide operates by the anti-resonance effect in the visible and near-infrared domain and includes a hollow core with defined gaps every 176 μm. The spectroscopic capabilities are demonstrated by various absorption-related experiments, showing that the Beer-Lambert law can be applied without any modification. In addition to revealing key performance parameters, time-resolved experiments showed a decisive improvement in diffusion times resulting from the lateral access provided by the microgaps. Overall, the microgap waveguide represents a pathway for on-chip spectroscopy in aqueous environments.

1. Introduction

1.1. Motivation and background

Spectroscopic methods are nowadays essential for a wide range of applications in fields such as bioanalytics or analytical chemistry. Here, miniaturization is playing an increasingly important role in combining these optical methods with microfluidic approaches, for example, to reduce geometric footprints and minimize sample volumes. In addition to light-scattering nanostructures (e.g., metasurfaces [1] or nanoantennas [2]), one attractive strategy focuses on integrated on-chip waveguides. Due to long light-matter interaction lengths, such waveguides can be used to detect small concentrations of analytes with high qualitative and quantitative accuracy [3–5]. Since water - by far the most important matrix liquid - has a refractive index (RI) lower than almost any solid material, total internal reflection cannot be used to guide light in water-filled waveguides. As a result, in the majority of cases, on-chip systems based on evanescent field waveguides are used. Here, the interaction with the analyte is provided by part of the optical mode penetrating a selected spatial domain outside the waveguide core (examples here are [6,7]). Although this

approach is widely used, it includes disadvantages: For instance the fraction of the field effectively interacting with the sample, which depends on the wavelength [8], is conventionally limited to a few percent, which demands long device lengths.

A conceptually better approach is to guide the light directly in the liquid sample using a hollow-core waveguide configuration. The key here is to compensate for the lack of total internal reflection by other light guiding mechanisms. Significant progress has been made recently in the field of fiber optics [9]: For example, the photonic bandgap effect has been applied to hollow-core fibers to minimize modal losses in air-filled fibers [10]. Recent developments in anti-resonant waveguides show even better performance [11], while the structural complexity is strongly reduced. It should be noted here that hollow-core fibers have been successfully employed in the context of liquid-based spectroscopy [12–14]. These examples clearly demonstrate the applicability of hollow-core structures and suggest that transferring established fiber-related concepts to planar systems can open up new fields of application for on-chip analytics.

The portfolio of established concepts for on-chip hollow-core waveguides is, however, substantially smaller. The most widespread concept to date are antiresonant reflective optical waveguides (ARROWs) [15]. Here, light is confined in the central waveguide regions through multilayer systems encapsulating a hollow core. Several applications in bioanalytics [16] and atomic spectroscopy [17] have been demonstrated.

A major problem of all planar and fiber hollow-core systems presented is the tubular geometry, which allows access to the optical core only through the end faces of the waveguides. This is particularly problematic in the case of diffusion-based exchange of analytes, as complete filling or removal of the analyte can lead to impractically long times. For example, filling a few centimeters long hollow-core fiber with alkali vapor requires duration of several months due to the low pressure [18,19].

An on-chip approach that uniquely combines lateral access and waveguiding in the core region is the recently introduced light cage [20]. Via 3D nanoprinting, structures consisting of a discrete number of spatially separated dielectric microstrands enclosing a central core domain have been demonstrated. The relevance of this structure in the context of spectroscopy has been demonstrated in various experiments [21,22]. Especially noteworthy is a quantum optical study where outstanding properties regarding gas diffusion could be demonstrated [23]. A new development in the field of on-chip hollow-core systems is the microgap waveguide [24]. This type of hollow-core waveguide is based on a square cross-section surrounded by submicron walls with defined interruptions every 200 μm for analyte exchange. The microgap waveguide uniquely combines the properties of conventional hollow core structures with lateral access. First gas-related experiments have demonstrated the relevance of this structure in the context of spectroscopy [24]. Here, we extend the field of application of microgap waveguides by demonstrating their implementation in optofluidics and liquid-based spectroscopy.

1.2. *This work*

In this study, the properties of the hollow-core microgap waveguide are investigated in the context of optofluidics and liquid-based spectroscopy. In addition to theoretical considerations of mode formation, the optical properties in aqueous environments were studied in the visible and near-infrared spectral domains in terms of transmission and influence of the refractive index environment. Furthermore, absorption specific characteristics by addition of a dye, as well as properties related to dye diffusion were revealed. In all cases, a very good agreement between calculations and experiments as well as to reference measurements was observed.

2.   Concept and design

2.1.   *Operational principle and waveguide design*

As shown in Ref. [24], the microgap waveguide confines light by the anti-resonance effect. This results in an alternating sequence of regions of high (transmission bands) and low (resonances) transmission in the spectral distribution of the waveguide power transmission [25]. The resonances originate from a modal anti-crossing of the central core mode with higher-order modes supported by the polymer walls. The spectral locations of these resonances can be estimated by the cut-off wavelengths of the respective higher-order mode of order m [26]. In the case of the microcap waveguide, this leads to the following equations for resonance wavelength [27]

$$\lambda_R = \frac{2w}{m}\sqrt{n_p^2 - n_l^2} \quad (m = 1, 2, ..) \tag{1}$$

Here, w is the wall thickness of the waveguide, while n_p and n_l refer to RIs of polymer and liquid, respectively. This equation emphasizes a particularly important feature of the microgap waveguide: Through engineering the wall thickness w, the spectral positions of the resonances λ_R can be tailored, which was exploited in the present work to shift one selected transmission band into the absorption domain of the analyte. Specifically, for the dye used here (Rhodamine 6G, R6G) the peak in the absorption spectrum is located at $\lambda = 527$ nm, so we chose a wall thickness of 1.55 μm. Based on preliminary experiments analyzing the modal losses, a core size of 20 μm and gap distance of 20 μm were selected, respectively, as shown in Fig. 1. Note that Eq. (1) also suggests a strong dependence of λ_R on the RI of the liquid n_m, which was investigated by exposing the waveguide to different volume fraction of Isopropanol (IPA) with DI-water.
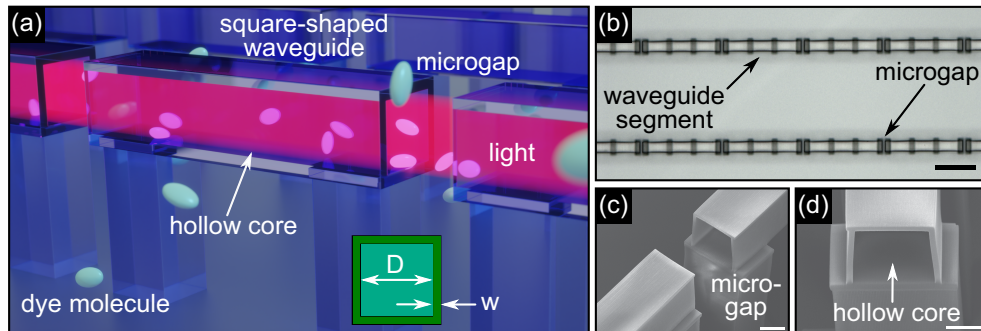
Fig. 1. The concept of the optofluidic square-shaped hollow-core microgap waveguide. (a) Illustration of the waveguide located in a water environment containing a dye. The inset represents the cross-section of the structure with two important parameters (core extent: D, wall thickness: w). (b) Optical microscopy image (top view) of a chip containing two waveguides (scale bar: 100 μm). The bottom SEM images show different views of the waveguide structure ((c): oblique front view showing a gap between two segments. (d) front view). In both SEM images, the scale refers to 10 μm.

2.2.   *Absorption in microgap waveguide*

In general, the linear absorption of light in a matrix transparent over the measurement length l and containing an absorbing species of concentration c (in mol/l) is given by the well-known Beer-Lambert law:

$$A = \epsilon(\lambda)cl \tag{2}$$

with the absorbance A and the wavelength-dependent molar attenuation coefficient of the analyte $\epsilon(\lambda)$ (in l/(mol·mm)). Note that $\epsilon(\lambda)$ is an intrinsic material parameter indicating how strongly a

selected species attenuates an electromagnetic wave at a given wavelength. As shown in one of our previous works [24], this law can be applied to the microgap waveguide without further modification. The reason for this is the large fraction of electromagnetic power in the core region (>99 %), being also a feature of the hollow-core light cage concept [20].

3. Methods

In the following, the experimental procedures used in this study (e.g., nanoprinting, preparation of the different solutions, etc.) and associated infrastructures are explained in this chapter. As a final point, the simulation method used is additionally introduced.

3.1. Nanoprinting

The waveguides were fabricated using a commercial laser direct writing system (Photonic Professional GT2, Nanoscribe GmbH, Germany) operating by two-photon polymerization (2PP). A 63 × objective (1.4 NA Oil DIC, Plan Apochromat, Zeiss) was inserted directly into the liquid resin (IP-DIP) located on silicon chip-based substrates. Note that the silicon chips were treated with a silanization process as applied in our previous work to prevent detachment [21]. In the first printing phase, fixed support posts were realized every 161 μm (geometric cross-section and height: 30 μm × 15 μm and 40 μm) to raise the waveguide from the substrate. These blocks are essential, since they (i) prevent residual excitation light reflected at the silicon substrate to impact the optical measurements and (ii) make slight tilts of the waveguide relative to the horizontal orientation of the nanoprinter, which can cause part of the waveguide to be printed inside the silicon substrate, negligible. Then, segments of the waveguide (length 176 μm) were printed onto the fixed support posts with a gap spacing of 20 μm. Depending on the experiments, the total length of the waveguides was adjusted between 0.5 cm and 1.5 cm. The laser power, scan speed, and hatch/slicing distance were 29 mW, 15000 μm/s, and 150 μm / 200 μm, leading to writing times of one complete microgap waveguide of 1.5/5 hours, respectively. In the final step, the printed structures were developed using 30 ml of propylene glycol methyl ether acetate (PGMEA, 99.9 % 484431 from Sigma Aldrich, Inc.) for 25 minutes and 30 ml of Purosovle 71/00 (from Puretecs) for 2 minutes. Finally, the samples were rinsed with IPA before the measurement.

3.2. Liquid solution preparation

To establish different RI environments, various mixtures of isopropanol (isopropyl alcohol, IPA, 99.9 % Carl Roth GmbH) and distilled water were prepared (IPA/water volume fraction: 0, 20, 40, 60, 70, 100 v/v %). The RI of the composite liquid can be found in one of our previous works [21]. Solutions containing defined concentrations of R6G (R4127 from Sigma-Aldrich, Inc.) were made with distilled water through diluting a highly concentrated solution (30 μM) to 15, 7.5, 3.75, 1.875, and 0.938 μM. Note that these solutions were also used in reference experiments. The absorption spectrum of each solution was controlled before the measurements using a UV-VIS spectrophotometer (V-666 from JASCO, Deutschland GmbH).

3.3. Fabrication of liquid chamber

The optofluidic chambers, which serve as reservoir wherein the waveguides are immersed, were designed in-house and implemented through standard low-resolution 3D printing (Agilista from Keyence Corp., photopolymer AR-M2). Sketches and a photo of the chamber are shown in Fig. S1 of the Supplementary Information. After printing, the chambers were cured, cleaned with DI-water and IPA, and dried out. The chamber (width: 2.0 cm, height: 1.0 cm, length: 1.5 cm, liquid volume used: ≈1 mL) consists of different parts: The base was combined with a commercially available high-precision waveguide launching stage. The windows were glued to

the chamber and were located on the front and back of the silicon chip. The silicon chips with the printed structures were fixed in the chamber using adhesive.

3.4.   Optical measurement setup

The optical setup (shown in Fig. SI2 of the supplementary information) was composed of a white light source (SuperK COMPACT, 450 nm $< \lambda <$ 2400 nm from NKT photonics GmbH), 20 × and 10 × objectives for in- and out-coupling, and high-precision launching stages. To remove the strong intensity of the pump laser, a notch filter with maximum absorption at 1065 nm (Edmund Optics) was inserted into the beam path before the sample. Preliminary measurements have shown that the remaining infrared light does not lead to any heating of the liquid and has no influence on the results. Reference measurements have been performed by moving the beam 500 µm above the waveguides (more details can be found in the Supplementary Information (Fig. SI1)). This procedure results in exactly the same interaction length in waveguide and reference experiments and therefore leads to a precise comparability of both measurements. The output was spectrally analyzed by an optical spectrum analyzer (AQ-6315A, Ando) connected to the multimode fiber (0.22 NA, FG050LGA from Thorlabs, Inc.), while the mode pattern was measured by a CCD camera (DCC1240C from Thorlabs, Inc.). The resulting spectra were normalized to the spectrum of the light source $T_{dB} = P_{waveg.}^{dBm} - P_{LS}^{dBm}$ with the transmitted power through the waveguide $P_{waveg.}^{dBm}$ and the power of the light source P_{LS}^{dBm} (both in units of dBm). To find the spectral locations of the transmission dips, the measured spectra were fitted by Gaussian functions within the vicinity of each individual resonance, allowing to extract the wavelength of minimal transmission (details can be found in Sec. 5 of the Supplementary Information (Fig. SI5)).

3.5.   Diffusion experiments

Time-resolved experiments were performed to reveal the properties of the microgap waveguide in terms of diffusion [21]. Here, monochromatic light at the main absorption line of R6G (λ = 527 nm) was coupled into a microgap waveguide (length 5 mm) located in an aqueous environment. In the next step, a defined amount of R6G (solution with 15 µM) was introduced into the distilled water and the transmitted power was acquired every 300 ms using a power meter. Thus, the diffusion of the dye into the waveguide core was measured in a time-resolved manner by following the decrease in light transmission resulting from the filling of the core with the absorbing species. The results were compared to reference measurements using capillaries of different core diameters. Note that compared to the absorption spectroscopic measurements, shorter samples (5 mm) were considered, as otherwise the diffusion time of the capillary sample can exceed practically feasible values.

3.6.   Simulations

The numerical calculations were performed with finite element modelling (FEM) based on commercial software tools (COMSOL Multiphysics and JCMwave). The behavior of the fundamental mode (HE_{11}) in the square cross-section was calculated at individual wavelengths across the entire relevant spectral range. As shown in our previous work [24], the impact of the gap on the dispersive properties of the fundamental mode can safely be neglected.

4.   Results

4.1.   Light guiding properties: spectral distribution of transmission

The first step for characterizing the light guidance properties was to measure the spectral distribution of the power transmission (Fig. 2(a)). In accordance to the typical behavior of antiresonant waveguides, an alternating sequence of spectral intervals with high and low

transmission could be observed, clearly confirming the aforementioned light guiding mechanism. This effect was further confirmed by the simulations (Fig. 2(b)), since the spectral positions of the anti-crossings, which result from the interaction of fundamental core mode with modes in the polymer walls, coincide with the transmission minima. Note the maximum fringe contrast of about 15 dB, which is an indicator of the high quality of the nanoprinted structures, and the high light transmission at $\lambda = 527$ nm, which was established by adjusting the wall thicknesses. The splitting of the resonances into two sub-dips is only observable in the experiment and could be explained by a small fabrication related difference in the thickness of opposing waveguide walls on the order of 50 nm [24]. The measured mode structure shows clear agreement with the calculated fundamental mode.
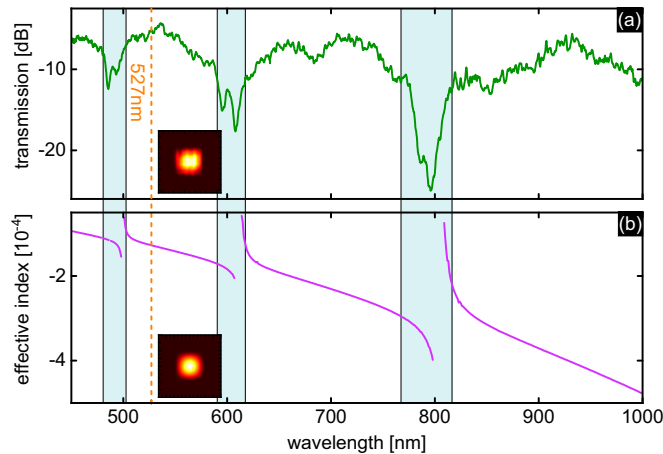
Fig. 2. Optical properties of the optofluidic microgap waveguide. (a) Measured spectral distribution of the transmission of the fundamental mode in a water environment. The inset shows the measured output mode profile at $\lambda = 525$ nm. (b) Simulated spectral distribution of the effective index of the fundamental mode relative to the index of water. The light blue areas show the correlation of the high loss regions and the simulated anti-crossings. The orange dashed vertical line indicates the main absorption wavelength of the dye ($\lambda = 527$ nm). The inset shows the simulated mode pattern at that wavelength.

4.2.   Light guiding properties: loss

To determine the optical losses, the transmitted power at the wavelength of maximum absorption of R6G ($\lambda = 527$ nm) of waveguides with five different lengths (5 mm to 15 mm) was investigated (Fig. SI3). As expected, the modal loss increases with waveguide length. The resulting losses, determined by the slope (dashed line), are 0.4 dB/mm, which are within the range of previous studies [28,29] and prove operation of the microgap waveguide in aqueous environment. The modes are excited here by means of an objective, leading to dominant excitation of the fundamental mode. Due to a similar modal structure, the coupling losses will be in the range obtained with air-filled waveguides. Using the data from Ref. [24], we determined these losses to be within between -2 dB and -6 dB.

4.3.   Refractive index dependence

Another important aspect regarding characterization is the dependence of the optical properties of the microgap waveguide on the environment, i.e., on the RI of the liquid. As described above, six RI scenarios were established by different mixtures of water and IPA (Fig. 3(b) shows the RI as a function of IPA concentration at $\lambda = 527$ nm) in the waveguide of length of 1.5

cm. The corresponding waveguide measurements (Fig. 3(a)) show an increasing blue shift of the transmission peaks for higher IPA concentrations, i.e., higher RIs. The wavelength of the transmission dips have been assigned to specific resonances using Eq. (1) by numerically determining the resonance wavelength λ_R for the different refractive index scenarios (i.e., different mixing ratios) taking into account the known wall thickness (here 1.468 µm). This analysis shows an almost perfect overlap of measurement results and theoretically expected resonance wavelength (Fig. 3(c)), thus a posteriori confirming the high accuracy of the dip determination procedure and underlining that the present structure uses the antiresonance effect as light guiding mechanism. Note that the fringe contrasts reach about 40 dB in the spectral domain 700 nm < λ < 750nm. In addition, it is important to note that no degradation of the optofluidic waveguide was observed over time, either in water or in IPA or in harsher environments (e.g., water/ethanol [30]), presumably because the structure is fully polymerized after development.
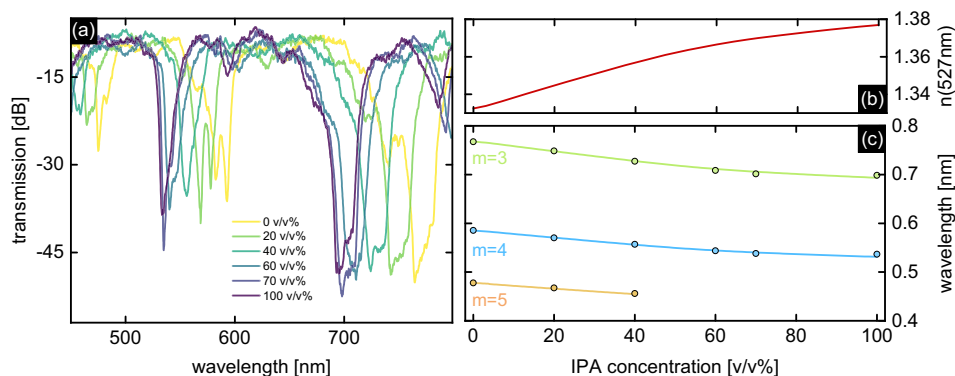
Fig. 3. Dependence of the optical properties of the optofluidic microgap waveguide on liquid environment (i.e., refractive index). (a) Spectral distribution of transmission of waveguide for different mixture ratios of water/IPA (indicated by the different colors). (b) Refractive index of water/IPA mixture as a function of IPA concentration at λ = 527 nm. (c) Spectral locations of measured transmission dips as a function of IPA concentration (points). The solid lines refer to simulations of the corresponding cutoff wavelength (i.e., resonance wavelength λ_R) determined by Eq. (1).

4.4. Integrated absorption spectroscopy: molar attenuation coefficient

To demonstrate the spectroscopic capabilities of the optofluidic microgap waveguide, different samples were exposed to aqueous environments of different concentrations of R6G, and spectrally resolved power transmission measurements were performed (Fig. 4(a)). A clear reduction in light transmission in the region of the dye absorption is visible, with this effect increasing for higher dye concentrations as expected. A key observation is the excellent overlap of the molar attenuation coefficient (defined in Sec. 2.2) between the waveguide measurements and reference measurements (the corresponding transmission spectra can be found in Sec. 4 of the Supplementary Information (Fig. SI4)) almost across the entire relevant spectral range (Fig. 4(b)). Note that measured values of molar attenuation coefficient both lie within the range of those reported in literature [31]. This agreement is also a a posteriori evidence for the direct application of the Beer-Lambert law, resulting from the high fraction of power in the waveguide core. Another key feature is the spectrally wide transmission bands covering almost the entire absorption range of the dye (light yellow areas in Fig. 4). It should be mentioned that the fine spectral features of the microgap waveguide are imprinted on the absorption spectrum, which, however, do not influence the result, i.e., the determination of the molar attenuation coefficient in any way.
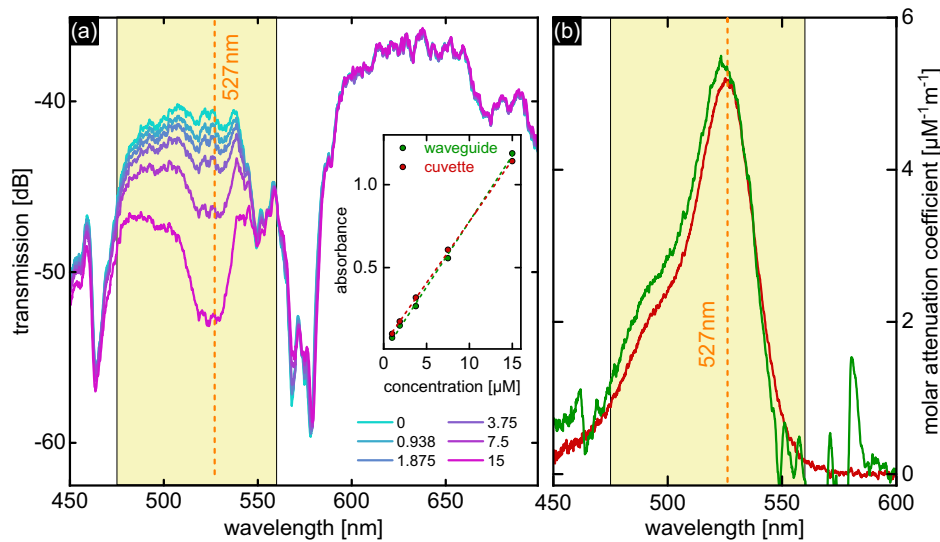
Fig. 4. Integrated absorption spectroscopy in the optofluidic microgap waveguide. (a) Spectral distribution of transmission of the waveguide in case the concentration of R6G in water is varied (each colored curve refers to one concentration, sample length: 1.5 cm). The inset is the calibration curve at the main absorption wavelength of the dye ($\lambda = 527$ nm), showing the absorbance vs. concentration (green: microgap waveguide, dark red: reference measurements). (b) Spectral distributions of the molar attenuation coefficient of R6G of 15 µM, obtained using the waveguide (green) in comparison to the corresponding reference (dark red). The orange dashed lines in (a) and (b) refer to the main absorption wavelength of R6G ($\lambda = 527$ nm), while the light yellow areas indicate the spectral interval of the main absorption of the R6G molecules.

4.5. Integrated absorption spectroscopy: limit of detection

The limit of detection (LoD) is an essential parameter for the comparison of spectroscopic systems and is defined here as LoD $= 3\sigma_A/m_A$ (σ_A: standard deviation of absorbance) in accordance with the Glossary Of Terms used in Photochemistry (3rd EDITION, IUPAC Recommendations 2006) [32]. The standard deviation σ_A [33,34] was determined by a statistical evaluation of 20 blank transmission measurements without analytes (microgap waveguide and reference with water only) following the procedure described in [32]. As R6G is used here, σ_A was determined at the main absorption line at $\lambda = 527$ nm. The slope parameter m_A was obtained by linear fitting of the individual data points of the transmission measurements (vertical dashed orange line in Fig. 4(a)), shown in the inset of Fig. 4(a), leading to the so-called calibration curve. The resulting data is summarized in Table 1, which allows a direct comparison to the reference measurements.

**Table 1. Summary of spectroscopic properties of optofluidic microgap waveguide and reference measurements.**

	microgap waveguide	reference measurements
slope of calibration curve m_A [µM^{-1}]	0.0791	0.0741
molar attenuation coefficient ϵ [µM^{-1}m^{-1}]	5.28	5.07
mean value of absorbance $\overline{A}$	0.448	0.469
standard deviation of absorbance σ_A	0.00198	0.00178
Limit-of-Detection [nM]	75	72

The results show nearly equal LoD values for microgap waveguide and reference measurements, emphasizing the quality of the nanoprinted structure and the applicability of the microgap waveguide concept within the context of spectroscopic applications. Note that the LoD depends not only on the waveguide itself, but also on the detection system used. Thus, it can be expected that improved diagnostics can further reduce the LoD. The minimum measured concentration in the experiments is $c = 0.93875$ μM for both waveguide and reference.

4.6. Integrated absorption spectroscopy: measured diffusion behavior

To reveal the influence of the gaps on the diffusion properties of the microgap waveguide from the experimental side, additional dynamic experiments were performed. As described in the Method section (Fig. SI1), a defined amount of R6G was introduced into the water-filled chamber containing a waveguide (gap size of 20 μm, length: 5 mm), and the transmitted power at the main absorption line of R6G was determined in a time time-resolved manner. The benchmark figure chosen here was the time after which the transmitted power dropped to 10% of the power before the addition of the dye ($t_{10\%}$). In the case of the microgap waveguide (Fig. 5) this time was about 2 minutes ($t_{10\%} = 2.4$ min), which is much shorter than those measured for a capillary having a comparable inner diameter ($t_{10\%} = 13.5$ min, diameter 20 μm). Note that even a capillary with a much larger diameter (224 μm) showed a longer diffusion time ($t_{10\%} = 6.9$ min). Thus, the results clearly show improved diffusion properties of the microgap waveguide compared to conventional systems that allow accessing the core only via the waveguide ports.
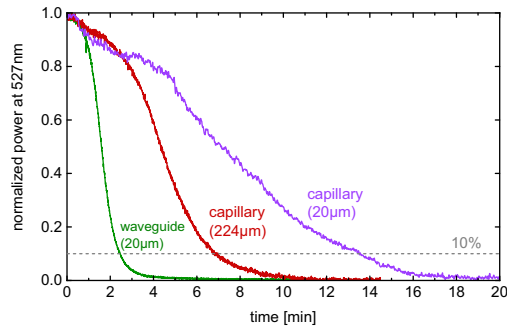
Fig. 5. Diffusion related properties of the optofluidic microgap waveguide. Transmitted power of monochromatic light ($\lambda = 527$ nm) through the optofluidic waveguide (green, gap size 20 μm , sample length 5 mm) and two capillaries of different core sizes (red: $D = 224$ μm, purple $D = 20$ μm) as a function of time (details can be found in the main text). The horizontal gray dashed line indicates the benchmark time at which the transmitted power has dropped to 10% of the power before addition of the dye. All curves have been normalized to the transmitted power at $t = 0$.

5. Discussion

5.1. Performance comparison to other waveguide solutions

In the following section, the performance of the optofluidic microgap hollow-core waveguide is placed in context with previously published works on waveguide-based integrated absorption spectroscopy. A direct comparison of the performance parameters of the different systems discussed below are summarized in Table 2.

Table 2. Comparison of the performance of the microgap waveguide with other waveguide systems used for absorption spectroscopy (yellow: this work, green: optofluidic hollow-core light cage, red: slab waveguide, blue: rib-type waveguide, gray: optical fiber)

Type of waveguide	Device Length	Cross-section (approx.)	Minimal C	LoD	Spectral domain	Ref.
Microgap waveguide	1.5 cm	20µm × 20µm	0.988µM in R6G	75nM in R6G	VIS	this work
Light cage	4.5 mm	24µm × 24µm	2µM in R6G	0.09µM in R6G	VIS	[21]
Slab waveguide	30 mm	16.7mm × 10mm	1µM in R6G	N.A	VIS	[35]
Slab waveguide	5 mm	20mm × 10mm	2.2µM in R6G	0.01µM in TNT	VIS	[36]
Planar nanoribbon	1.5 mm	D = 150nm & 200nm	6µM in R6G	0.3mM in EITC (eosin-5-isothiocyanate)	VIS	[37]
Polymer core waveguide	11cm	40µm × 50µm	Unknown	N.A	VIS	[38]
Liquids core fiber	130 cm	D = 1mm	0.13nM in R6G	N.A	VIS	[39]
Hollow core fiber	100 cm	D = 30µm	0.1µM in SMX	0.05µM in SMX	UV-VIS	[14]

5.2. Comparison with light cage

The key system for comparison is the optofluidic light cage, which was introduced by the authors in 2018 [20] and investigated with respect to microfluidic absorption spectroscopy in 2021 [21]. Having similar core dimensions, the microgap waveguide shows a better LoD (microgap: 75 nM, light cage: 90 nM), which is possibly due to the longer light-liquid interaction length (light cage: 5 mm, microgap waveguide: 15 mm). Noteworthy is also a similar diffusion time of both systems (microgap: 2.4 min, light cage: 2.1 min). This leads to an advantage for the microgap waveguide in terms of implementation, as it includes a rectangular symmetry compared to the round elements of the light cage, which is easier, faster and more precise to print. Furthermore, the microgap waveguide used here exhibits wider transmission bands ($\Delta\lambda \approx 100$ nm), which in the present case cover almost the entire absorption range of the dye. In contrast, for the light cage, the thick polymer strands lead to a higher density of strand modes and thus much narrower transmission windows ($\Delta\lambda \approx 50$ nm) [26,28]. Note that, as shown in Ref. [24], the maximum spectral extent of a transmission band achieved so far for the microgap waveguide is $\Delta\lambda \approx 200$ nm. Note that light cages and microgap waveguides were repeatedly exposed to different liquid environments without degradation or change in optical properties, which emphasizes their stability and robustness.

5.3. Other planar systems

Another category of relevant systems are evanescent field-based slab and ridge waveguides [35,–38], which overall exhibit similar performance parameters compared to the microgap waveguide (Table 2). Note that a key advantage of the microgap waveguide (and light cage) is that the light-matter interaction occurs within a hollow core. In contrast, in evanescent field-based systems, the interaction takes place near a surface, which can lead to undesirable effects. For example, undesired absorption features were measured in [35], resulting from dimer formation near a surface. Such an effect was not observed in the microgap waveguide and light cage experiments, which renders additional surface treatment unnecessary.

5.4. Hollow core fibers

Optical fibers with liquid cores are another class of relevant systems the microgap waveguide should be compared to. For example, Teflon is used as a cladding material to guide light directly in water due to its very low refractive index [39]. However, the massive intrinsic surface roughness necessitates very large core diameters in the millimeter range to compensate for the scattering losses. Another relevant type of fiber with greater structural complexity are antiresonant hollow core fibers, which are used, for example, to detect pharmaceuticals in water through UV spectroscopy [14]. The performance achieved lies in the range of the microgap waveguide, although much longer sample lengths (fiber length 1 m) are required.

5.5. Application in nanoparticle tracking analysis

One area where the diffusion-related properties of microgap waveguides can be beneficial is in nanoparticle tracking analysis (NTA). As shown in a recently published work [30] nanoprinted light cages can be employed for measuring the solvency-induced collapse of a nanoparticle system that reacts to changes in the liquid environment. Due to the comparably simpler geometry of microgap waveguides and particularly the non-rounded surfaces of the nanoprinted elements, substantially improved microscopic imaging properties of the individual nanoparticles can be expected, which is crucial in particular when tracking nanoscale species. In addition, the tube-type geometry of the microgap waveguide impedes transverse diffusion of the nanoparticles, allowing them to be observed for very long durations, thus overall improving NTA-statistics.

6. Conclusion

Miniaturization of spectroscopic approaches using integrated on-chip systems represents a major research direction in the field of analytics. In this work, we uncover the properties of the on-chip hollow-core microgap waveguide in the context of optofluidics that enables intense light-analyte interaction over long lengths and fast response times through lateral accesses. The structure consists of a square-shaped hollow core surrounded by a micrometer-thick polymer wall with defined gaps every 180 μm along the waveguide axes for accessing the core. 3D nanoprinting was used for implementing structures on silicon chips, which does not require any further post-processing steps. In the case of an aqueous environment, the anti-resonance effect was clearly identified as the light guiding mechanism, with measurements suggesting an excellent quality of the implemented structures (e.g., 40 dB fringe contrast). The absorption spectroscopic capabilities were demonstrated using R6G as an example. Here, excellent agreement was shown between reference and waveguide measurement over the entire relevant spectral range. This resulted from the extremely high fraction of the field in the core ($> 99\%$), which allows a direct application of the Beer-Lambert law without any modification. In contrast, evanescent field waveguides require lengthy calculations of the modal properties to determine a wavelength-dependent correction term to account for the large fraction of electromagnetic power that is not guided in the analyte. Furthermore, it is important to note that the used transmission band covers almost the entire

absorption range of the dye.The determined performance parameters are overall better than those of the light cage and are in the range of comparable systems, while the design is considerably simpler. Time-resolved experiments on dye diffusion showed a decisive influence of the microgap with much shorter diffusion times compared to tubular waveguide systems.

Overall, the microgap waveguide represents a promising integrated approach for on-chip water-based absorption spectroscopy with excellent performance parameters. In addition to absorption spectroscopy, further applications in areas such as Raman spectroscopy or bioanalytics (e.g. nanoparticle tracking analysis) can be foreseen. The possibility of further integration by interfacing the waveguide with optical fibers should be mentioned, which could be shown for the light cage structure [22] and can theoretically be transferred to the microgap waveguide.

Disclosures. The authors declare no conflicts of interest.

Data availability. The data that support the findings of this study are available from the authors upon reasonable request.

Supplemental document. See Supplement 1 for supporting content.

References

1. S. Zhang, C. L. Wong, S. Zeng, R. Bi, K. Tai, K. Dholakia, and M. Olivo, "Metasurfaces for biomedical applications: imaging and sensing from a nanophotonics perspective," Nanophotonics **10**(1), 259–293 (2021).
2. A. Habib, X. Zhu, S. Fong, and A. A. Yanik, "Active plasmonic nanoantenna: an emerging toolbox from photonics to neuroscience," Nanophotonics **9**(12), 3805–3829 (2020).
3. F. S. Ligler, M. Breimer, J. P. Golden, D. A. Nivens, J. P. Dodson, T. M. Green, D. P. Haders, and O. A. Sadik, "Integrating waveguide biosensor," Anal. Chem. **74**(3), 713–719 (2002).
4. W.-J. Kim, B. K. Kim, A. Kim, C. Huh, C. S. Ah, K.-H. Kim, J. Hong, S. H. Park, S. Song, J. Song, and G. Y. Sung, "Response to cardiac markers in human serum analyzed by guided-mode resonance biosensor," Anal. Chem. **82**(23), 9686–9693 (2010).
5. W. Budach, A. P. Abel, A. E. Bruno, and D. Neuschäfer, "Planar waveguides as high-performance sensing platforms for fluorescence-based multiplexed oligonucleotide hybridization assays," Anal. Chem. **71**(16), 3347–3355 (1999).
6. P. Xiao, X. Wang, J. Sun, H. Li, M. Huang, X. Chen, and Z. Cao, "Biosensor based on hollow-core metal-cladding waveguide," Sens. Actuators, A **183**, 22–27 (2012).
7. V. J. Cadarso, C. Fernández-Sánchez, A. Llobera, M. Darder, and C. Domínguez, "Optical biosensor based on hollow integrated waveguides," Anal. Chem. **80**(9), 3498–3501 (2008).
8. B. Doherty, A. Csáki, M. Thiele, M. Zeisberger, A. Schwuchow, J. Kobelke, W. Fritzsche, and M. A. Schmidt, "Nanoparticle functionalised small-core suspended-core fibre–a novel platform for efficient sensing," Biomed. Opt. Express **8**(2), 790–799 (2017).
9. W. Belardi, "Hollow-core optical fibers," Fibers **7**(5), 50 (2019).
10. F. Poletti, M. N. Petrovich, and D. J. Richardson, "Hollow-core photonic bandgap fibers: technology and applications," Nanophotonics **2**(5-6), 315–340 (2013).
11. H. Sakr, Y. Chen, G. T. Jasion, T. D. Bradley, J. R. Hayes, H. C. H. Mulvad, I. A. Davidson, E. Numkam Fokoua, and F. Poletti, "Hollow core optical fibres with comparable attenuation to silica fibres between 600 and 1100 nm," Nat. Commun. **11**(1), 6030 (2020).
12. A. M. Cubillas, M. Schmidt, M. Scharrer, T. G. Euser, B. J. M. Etzold, N. Taccardi, P. Wasserscheid, and P. S. J. Russell, "Ultra-low concentration monitoring of catalytic reactions in photonic crystal fiber," Chem. - Eur. J. **18**(6), 1586–1590 (2012).
13. A. M. Cubillas, S. Unterkofler, T. G. Euser, B. J. M. Etzold, A. C. Jones, P. J. Sadler, P. Wasserscheid, and P. S. J. Russell, "Photonic crystal fibres for chemical sensing and photochemistry," Chem. Soc. Rev. **42**(22), 8629–8648 (2013).
14. M. Nissen, B. Doherty, J. Hamperl, J. Kobelke, K. Weber, T. Henkel, and M. A. Schmidt, "UV absorption spectroscopy in water-filled antiresonant hollow core fibers for pharmaceutical detection," Sensors **18**(2), 478 (2018).
15. D. Yin, H. Schmidt, J. P. Barber, and A. R. Hawkins, "Integrated arrow waveguides with hollow cores," Opt. Express **12**(12), 2710–2715 (2004).
16. G. Testa, G. Persichetti, and R. Bernini, "Liquid core arrow waveguides: a promising photonic structure for integrated optofluidic microsensors," Micromachines **7**(3), 47 (2016).
17. W. Yang, D. B. Conkey, B. Wu, D. Yin, A. R. Hawkins, and H. Schmidt, "Atomic spectroscopy on a chip," Nat. Photonics **1**(6), 331–335 (2007).

18. M. Sprague, P. Michelberger, T. Champion, D. England, J. Nunn, X.-M. Jin, W. Kolthammer, A. Abdolvand, P. S. J. Russell, and I. Walmsley, "Broadband single-photon-level memory in a hollow-core photonic crystal fibre," Nat. Photonics **8**(4), 287–291 (2014).

19. K. T. Kaczmarek, D. J. Saunders, M. R. Sprague, W. S. Kolthammer, A. Feizpour, P. M. Ledingham, B. Brecht, E. Poem, I. A. Walmsley, and J. Nunn, "Ultrahigh and persistent optical depths of cesium in kagomé-type hollow-core photonic crystal fibers," Opt. Lett. **40**(23), 5582–5585 (2015).

20. C. Jain, A. Braun, J. Gargiulo, B. Jang, G. Li, H. Lehmann, S. A. Maier, and M. A. Schmidt, "Hollow core light cage: trapping light behind bars," ACS Photonics **6**(3), 649–658 (2018).

21. J. Kim, B. Jang, J. Gargiulo, J. Bürger, J. Zhao, S. Upendar, T. Weiss, S. A. Maier, and M. A. Schmidt, "The optofluidic light cage–on-chip integrated spectroscopy using an antiresonance hollow core waveguide," Anal. Chem. **93**(2), 752–760 (2020).

22. B. Jang, J. Gargiulo, J. Kim, J. Bürger, S. Both, H. Lehmann, T. Wieduwilt, T. Weiss, S. A. Maier, and M. A. Schmidt, "Fiber-integrated hollow-core light cage for gas spectroscopy," APL Photonics **6**(6), 061301 (2021).

23. F. Davidson-Marquis, J. Gargiulo, E. Gómez-López, B. Jang, T. Kroh, C. Müller, M. Ziegler, S. Maier, H. Kübler, M. Schmidt, and O. Benson, "Coherent interaction of atoms with a beam of light confined in a light cage," Light: Sci. Appl. **10**, 1–10 (2021).

24. J. Bürger, V. Schalles, J. Kim, B. Jang, M. Zeisberger, J. Gargiulo, L. de S. Menezes, M. A. Schmidt, and S. A. Maier, "3D-nanoprinted antiresonant hollow-core microgap waveguide: An on-chip platform for integrated photonic devices and sensors," ACS Photonics **9**(9), 3012–3024 (2022).

25. M. Zeisberger and M. A. Schmidt, "Analytic model for the complex effective index of the leaky modes of tube-type anti-resonant hollow core fibers," Sci. Rep. **7**(1), 11761 (2017).

26. B. Jang, J. Gargiulo, R. F. Ando, A. Lauri, S. A. Maier, and M. A. Schmidt, "Light guidance in photonic band gap guiding dual-ring light cages implemented by direct laser writing," Opt. Lett. **44**(16), 4016–4019 (2019).

27. N. M. Litchinitser, S. C. Dunn, B. Usner, B. J. Eggleton, T. P. White, R. C. McPhedran, and C. M. de Sterke, "Resonances in microstructured optical waveguides," Opt. Express **11**(10), 1243–1251 (2003).

28. J. Bürger, J. Kim, B. Jang, J. Gargiulo, M. A. Schmidt, and S. A. Maier, "Ultrahigh-aspect-ratio light cages: fabrication limits and tolerances of free-standing 3D nanoprinted waveguides," Opt. Mater. Express **11**(4), 1046–1057 (2021).

29. B. Jang, J. Gargiulo, M. Ziegler, R. F. Ando, U. Hübner, S. A. Maier, and M. A. Schmidt, "Fine-tuning of the optical properties of hollow-core light cages using dielectric nanofilms," Opt. Lett. **45**(1), 196–199 (2020).

30. J. Kim, R. Förster, T. Wieduwilt, B. Jang, J. Bürger, J. Gargiulo, L. de S. Menezes, C. Rossner, A. Fery, S. A. Maier, and M. A. Schmidt, "Locally structured on-chip optofluidic hollow-core light cages for single nanoparticle tracking," ACS Sens. **7**(10), 2951–2959 (2022).

31. H. Du, R.-C. A. Fuh, J. Li, L. A. Corkan, and J. S. Lindsey, "PhotochemCAD: A computer-aided design and research tool in photochemistry," Photochem. Photobiol. **68**, 141–142 (1998).

32. S. E. Braslavsky, "Glossary of terms used in photochemistry, (IUPAC recommendations 2006)," Pure Appl. Chem. **79**(3), 293–465 (2007).

33. A. Shrivastava and V. B. Gupta, "Methods for the determination of limit of detection and limit of quantitation of the analytical methods," Chron. Young Sci. **2**(1), 21–25 (2011).

34. D. A. Armbruster and T. Pry, "Limit of blank, limit of detection and limit of quantitation," The Clinical Biochemist Reviews **29**, S49 (2008).

35. N. Matsuda, A. Takatsu, and K. Kato, "Absorption spectra of rhodamine 6G by slab optical waveguide spectroscopy," Chem. Lett. **25**(2), 105–106 (1996).

36. P. Liu, Z. Li, B. Li, G. Shi, M. Li, D. Yu, and J. Liu, "The analysis of time-resolved optical waveguide absorption spectroscopy based on positive matrix factorization," J. Colloid Interface Sci. **403**, 134–141 (2013).

37. D. J. Sirbuly, A. Tao, M. Law, R. Fan, and P. Yang, "Multifunctional nanowire evanescent wave optical sensors," Adv. Mater. **19**(1), 61–66 (2007).

38. L. Jiang and S. Pau, "Integrated waveguide with a microfluidic channel in spiral geometry for spectroscopic applications," Appl. Phys. Lett. **90**(11), 111108 (2007).

39. L. Kröckel, T. Frosch, and M. A. Schmidt, "Multiscale spectroscopy using a monolithic liquid core waveguide with laterally attached fiber ports," Anal. Chim. Acta **875**, 1–6 (2015).